Total Surface Current Vector and Shear From a Sequence of Satellite Images: Effect of Waves in Opposite Directions

Fabrice Ardhuin, Matias Alday, Maria Yurovskaya

JGR Oceans

RESEARCH ARTICLE
10.1029/2021JC017342

Special Section:
Remote sensing of ocean surface currents using Doppler techniques from planes and satellites

Key Points:

- Phase shifts in lagged pairs of satellite images yield information on near-surface current and shear
- Waves in opposite directions can corrupt current estimates in particular for wavelengths under 25 m
- A sequence of three images gives a separation of waves in opposing direction and a current estimate

Correspondence to:
F. Ardhuin,
ardhuin@ifremer.fr

Citation:
Ardhuin, F., Alday, M., & Yurovskaya, M. (2021). Total surface current vector and shear from a sequence of satellite images: Effect of waves in opposite directions. *Journal of Geophysical Research: Oceans*, *126*, e2021JC017342. https://doi.org/10.1029/2021JC017342

Received 10 MAR 2021
Accepted 10 JUN 2021

Total Surface Current Vector and Shear From a Sequence of Satellite Images: Effect of Waves in Opposite Directions

Fabrice Ardhuin[1,2], Matias Alday[1], and Maria Yurovskaya[3,4]

[1]Laboratoire d'Océanographie Physique et Spatiale, CNRS, Ifremer, IRD, University of Brest, Brest, France, [2]Scripps Institution of Oceanography, University of California San Diego, La Jolla, CA, USA, [3]Marine Hydrophysical Institute of RAS, Sevastopol, Russia, [4]Russian State Hydrometeorological Institute, St. Petersburg, Russia

Abstract The total surface current velocity (TSCV)—the horizontal vector quantity that advects seawater—is an essential climate variable, with few observations available today. The TSCV can be derived from the phase speed of surface gravity waves, and the estimates of the phase speeds of different wavelengths could give a measure of the vertical shear. Here, we combine 10-m resolution Level-1C of the Sentinel-2 Multispectral Instrument, acquired with time lags up to 1 s, and numerical simulation of these images. Retrieving the near-surface shear requires a specific attention to waves in opposing directions when estimating a single-phase speed from the phase difference in an image pair. Opposing waves lead to errors in phase speeds that are most frequent for shorter wavelengths. We propose an alternative method using a least squares fit of the current speed and amplitudes of waves in opposing directions to the observed complex amplitudes of a sequence of three images. When applied to Sentinel-2, this method generally provides more noisy estimate of the current. A byproduct of this analysis is the "opposition spectrum" which is a key quantity in the sources of microseisms and microbaroms. For future possible sensors, the retrieval of TSCV and shear can benefit from increased time lags, resolution, and exposure time of acquisition. These findings should allow new investigations of near-surface ocean processes including regions of freshwater influence or internal waves, using existing satellite missions such as Sentinel-2, and provide a basis for the design of future optical instruments.

Plain Language Summary Measuring ocean surface current and its vertical variation is important for a wide range of science questions and applications. A well-known technique for measuring currents from ocean surface images is to follow the motion of wave crests from one image to another, measuring their celerity. The values obtained for different wavelengths give access to an estimate of the current at different depths. When using only two images, the technique breaks down if there are waves traveling in opposing directions with comparable energy levels. We show that this is generally a problem for shorter wave components because there are generally waves in opposing directions with significant energy for wavelengths shorter than 25 m. Here, we generalize the technique to a sequence of three images that allows to separate the waves in opposing directions. Applications of this method to existing data from the Sentinel-2 satellite is difficult due to short time differences between image acquisitions. Several improvements on the Sentinel-2 sensor are proposed for a specific instrument that would measure surface current and shear.

1. Introduction

Surface current velocities play an important role in many ocean processes, including the flux of kinetic energy from the atmosphere to the ocean (Wunsch & Ferrari, 2009), air-sea fluxes (Cronin et al., 2019), and the transport of buoyant material (Maximenko et al., 2019). Different observation systems have been proposed to measure the surface current in a wide range of conditions. Barrick (1977) and many others have developed land-based HF radars that rely on the dispersion relation of surface gravity waves, while open ocean conditions are very sparsely monitored by a wide range of techniques that differ in their effective depth of measurement, as illustrated in Figure 1. In situ moorings are typically limited to measurements at depths larger than 5 m, away from the layer where the Stokes drift of surface gravity waves is strong. In particular, surface velocity program (SVP) drifters have been designed to have the least influence of wave

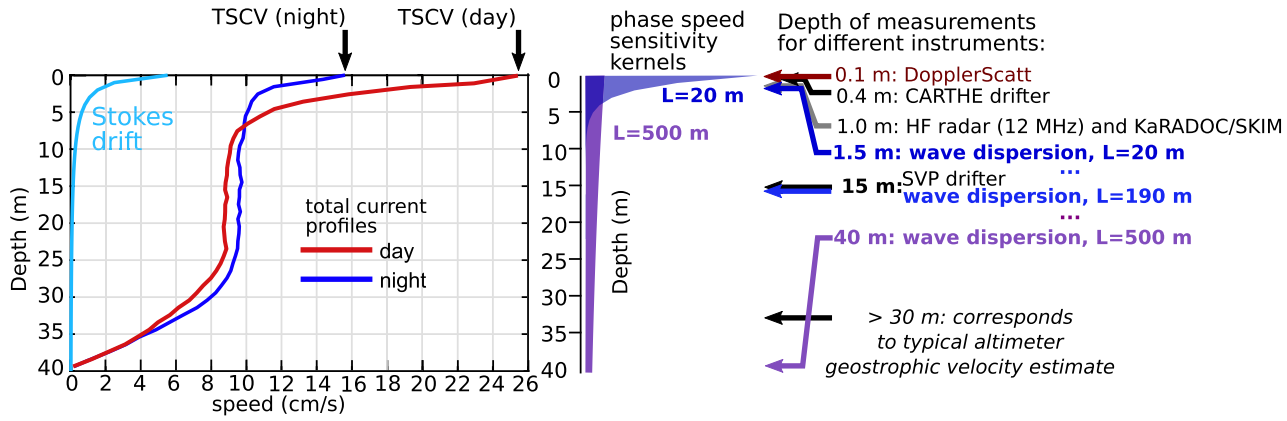

Figure 1. Left: typical day and night velocity profiles of the total current in the Atlantic at 26°N, 36°W (adapted from Sutherland et al. [2016]). Center: sensitivity kernels for surface gravity wave phase speeds. Right: depth of measurement of different instruments. From top to bottom: DopplerScatt (Rodríguez et al., 2018), CARTHE drifters (Novelli et al., 2017), HF radars at 12 MHz (Stewart & Joy, 1974), near nadir Ka-band radars such as KaRADOC (Marié et al., 2020). The depth of measurement for wave dispersion is taken as the depth where a linear velocity profile matches the contribution of the current to the phase speed, namely $z = 0.08\,L$ where L is the considered wavelength (Stewart & Joy, 1974; Teague et al., 2001).

motions in their measurements thanks to a drogue centered around 15 m depth (Lumpkin et al., 2017; Niiler & Paduan, 1995). In the absence of that drogue, the drifter measures a not so clear combination of wind and surface current speeds (Elipot et al., 2016). The surface drifts of Argo floats have also been used (Lebedev et al., 2007), and, for the lack of a better alternative, satellite remote sensing can be used, combining scatterometer winds, sea level anomalies from altimeters, and a combination of in situ drifters and satellite gravimeters for the Mean Dynamic Topography (Rio et al., 2014).

These estimates of the near-surface current can have significant differences, in part due to the sampling of different depths, as illustrated in Figure 1. Each measurement system provides a horizontal current velocity that is a convolution of the vertical profile of the velocity. For simplicity, it is convenient to define a "measurement depth" that can be taken as the depth at which a linearly varying current takes the given value. We note that DopplerScatt involves an empirical Geophysical Model Function and thus the physics of the measurement are not completely understood but the backscatter dominated by short gravity waves suggests a measurement depth under 0.1 m, whereas near-nadir radar measurements, such as performed by the KaRADOC instrument (Marié et al., 2020) give a velocity that is weighted by the surface slope spectrum and corresponds to a measurement depth that does not vary much around 1 m. It is thus desirable to measure the vertical shear of the current in order to be able to compare or combine these estimates from different observing systems. The shear is also an important indication of mixing or lack thereof, giving information on possible upper-ocean stratification.

Shear estimates have used the wave dispersion modification due to the current vector, defined by the two components $U_x(z)$ and $U_y(z)$ of the horizontal current profile (Stewart & Joy, 1974). For completeness, a nonlinear wave correction should also be included (Ardhuin et al., 2009; Broche et al., 1983), which is almost the same as replacing the Eulerian mean current by the Lagrangian mean current (Andrews & McIntyre, 1978). We thus expect, for $kD \gg 1$,

$$U(k,\varphi) \simeq U(k)\cos(\varphi - \varphi_U) = 2k \int_{-D}^{0} U_x(z)\exp(2kz)\cos\varphi + U_y(z)\exp(2kz)\sin\varphi \mathrm{d}z. \quad (1)$$

Obtaining current shear from a sequence of images has been done from many sensors, including stereo-video imagery (Fedele et al., 2013), X-band radar (Campana et al., 2016), or polarimetric imagery (Laxague et al., 2018). In all cases, it requires reliable estimates of $U(k, \varphi)$, for different wavelengths, including the shortest components, and this is performed by identifying propagating waves in the three-dimensional (3D) Fourier transform of the measured signals (Peureux et al., 2018; Young et al., 1985). A great opportunity is offered by satellite imagery with accurately co-registered views of the same ocean surface with short time lags. This is particularly the case of Sentinel-2 imagery has been used to estimate surface current

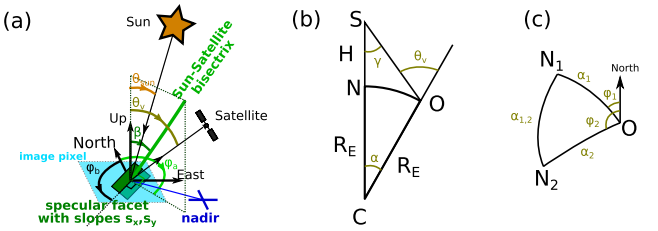

Figure 2. (a) Definition of viewing angles corresponding to a given sun and satellite sensor positions. The image brightness of a pixel is defined by the area of sub-pixel facets (in green) that gives a specular reflection and thus must have a given surface slope vector (s_x, s_y). That area is proportional to the probability density function within that pixel for the slope (s_x, s_y). This slope corresponds to the zenith angle β and azimuth φ_a. The perpendicular azimuths $\varphi_b = \varphi_a \pm \pi/2$ are "blind azimuths" in which the waves contribute a second-order change to the pixel brightness and cannot be observed. (b) Position of satellite (S), observation point (O), and center of the Earth (c) in a vertical plane. (c) Triangle on the sphere joining the observation point O and the nadir positions N_1 and N_2 at observation times 1 and 2.

(Kudryavtsev et al., 2017b). The Sentinel-2 Multispectral Instrument (Drusch et al., 2012) has very strict co-registration requirements that make it possible to observe the signature of current velocities of the order of 1 m/s (Yurovskaya et al., 2019). Compared to methods that use a series of many images processed with a 3D Fourier transform, the analysis of only a few images is more difficult because of the very poor temporal resolution that does not give a full spectrum in the frequency domain. In particular, the linear wave signal is not so easily separated from other contributions to the measurement.

The objective of the present study is to discuss the influence of this limited time sampling on the accuracy of surface current estimates, in the presence of waves propagating in opposing directions, starting with the two-image method used by Kudryavtsev et al. (2017b), as discussed in Section 2. To demonstrate the different processing steps and the influence of the image properties, we rely on the comparison of true data and simulated images generated using the simulator described in Appendix A. Due to the possible corruption of phase speeds by waves in opposing directions, we propose a new method using sequences of three images, as described in Section 3 with details given in Appendix B. Discussions and conclusions follow in Sections 4 and 5. This study does not address issues associated with systematic errors in the spatial registration on a global reference system with subpixel accuracy. These are partly discussed in Kääb et al. (2016) and Yurovskaya et al. (2019) and will be the topic of future work.

2. Effect of Waves in Opposite Directions With Two-Image Sun Glint Method

2.1. Short Waves in Opposing Directions

Pictures of the sun glint reveal wave patterns that are caused by the tilting of the sea surface by waves with wavelength larger than the pixel, adding their long wave slope to the local slope probability density function, and thus changing the pixel brightness. This effect has been described in many studies including Kudryavtsev et al. (2017a), and the geometry of the measurement is defined in Figure 2. A key concept is that the surface can be decomposed in facets with a size of the order of 1 mm by 1 mm, scale at which the sea surface is well approximated by a plane. There are thus a large number of such facets in a typical image pixel (10 m by 10 m for some of the bands of the MSI sensor on Sentinel-2), but the number of those that correspond to the specular direction can be relatively small, of the order of 100, while their brightness also varies, introducing random fluctuations in the image brightness.

As shown in Figure 2b for a spherical Earth, the satellite position S and observation point O correspond to a zenithal angle θ_v, related to the off-nadir angle γ by the law of sines,

$$\sin\gamma \,/\, R_E = \sin(\pi - \theta_v) \,/\, (R_E + H). \tag{2}$$

The time of acquisition of the different pixels is not available in the Level-1C Sentinel-2 product, but it can be retrieved from the provided view geometry. For example, color band B01 is acquired at time t_1 when B02 is acquired at time t_2, the time difference is given by the ratio of the angular distance $\alpha_{1,2}$ between the two nadir points N_1 and N_2, as depicted in Figure 2c, and the angular speed along the orbit Ω (in rad/s). The angular distance $\alpha_{1,2}$ is obtained from the law of cosines on the sphere,

$$\cos\alpha_{1,2} = \cos\alpha_1 \cos\alpha_2 + \sin\alpha_1 \sin\alpha_2 \cos(\varphi_2 - \varphi_1). \tag{3}$$

This typically gives distances and time lags within 1% of the expression given by Equation 1 in Yurovskaya et al. (2019).

To illustrate the limitations of the two-image method, we start from the same image example that was used in Kudryavtsev et al. (2017a), acquired off the California coast in the region of San Diego. The image

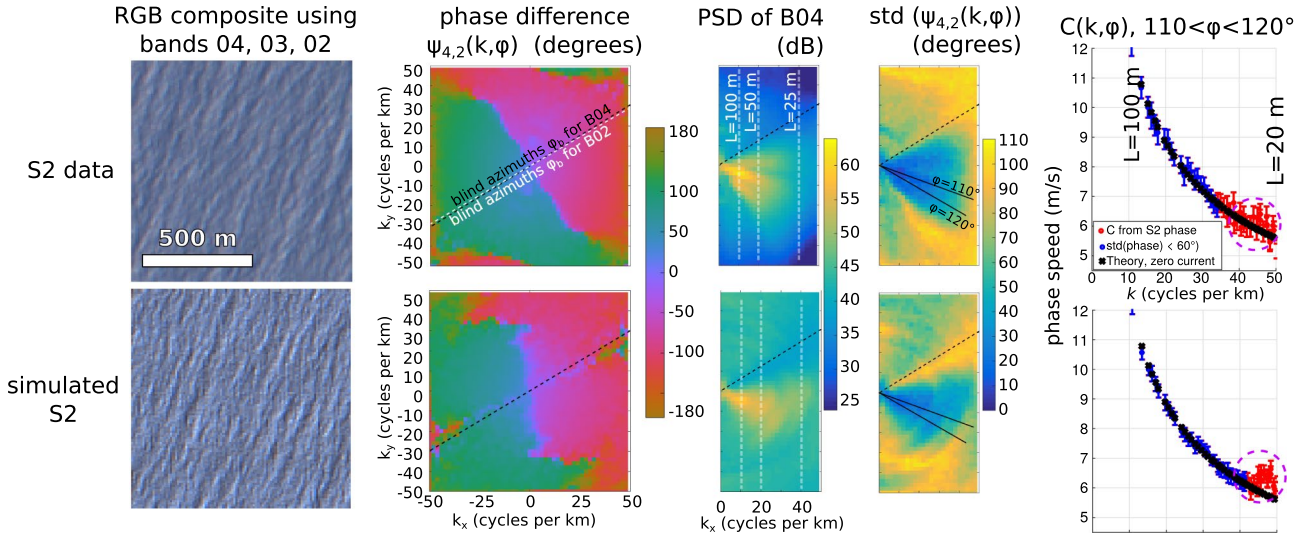

Figure 3. Example of processing from Level-1C images to phase speeds, using 500 × 500 m^2 tiles over an 8 by 8 km area. Top: data from Copernicus Sentinel-2 on April 29, 2016, off California (see Figures 3–9 in Kudryavtsev et al. [2017a, 2017b]), with $\beta = 9°$, $U_{10} = 6$ m/s. Bottom: simulated Sentinel-2 data based on in situ wave spectrum determined from directional moments using the maximum entropy method (MEM), and with random phases. The multiplicative noise amplitude is set to $N_t = 0.15$. The present paper was motivated by the phase speed anomalies, highlighted with the dashed magenta circle near the Nyquist wavelength $L = 20$ m.

processing method is illustrated in Figure 3. To understand the processing results, we also have generated simulated images and applied the exact same processing to them.

The image simulator is described in more detail in Appendix A, and corresponds to the forward model of Kudryavtsev et al. (2017a), combined with a noise model. For our first example, the model input parameters are the Sentinel-2 viewing geometry, an estimate of the surface wind vector given by satellite scatterometer data, and a directional wave spectrum that is estimated from an in situ buoy. The buoy is station number 220 of the Coastal Data Information Program (CDIP) located at 32.752°N 117.501°W, also identified by the World Meteorological Organization with the number 46258.

To obtain a more robust estimation of the current speed, we used a phase estimated from the coherent sum of the complex amplitudes obtained from individual image tiles that are 500 m wide. We first sum the $16^2 = 256$ tiles, and then add 15^2 tiles that are shifted by 250 m in each direction to use the signal that is otherwise much reduced by the two-dimensional Hann window, but is these shifted windows are not independent samples. This gives 256 independent estimates of the phase and associated current for each spectral component. The main information that we shall use is the phase difference $\psi_{i,j}(k, \varphi)$ between the bands number i and j, for the spectral component with wavenumber k propagating in azimuth φ.

By definition the phase changes sign for opposite directions $\psi_{i,j}(k, \varphi) = -\psi_{i,j}(k, \varphi + \pi)$, and this phase difference can be interpreted as the result of the propagation of a single wave component at speed

$$C(k,\varphi) = \psi_{i,j}(k,\varphi) \,/\, [k(t_i - t_j)], \tag{4}$$

where t_i is the acquisition time for band i. Most of our analysis of Sentinel-2 data is based on the bands B04 and B02 giving a phase $\psi_{4,2}(k,\varphi)$.

The shortest waves that propagate along the x or the y axis in the image have a 20 m wavelength. Their phase speed, for zero current, is expected to be 5.6 m/s and thus the wave patterns should be displaced by 5.6 m between the red and the blue channels that are separated by 1.0 s, and only 2.8 m between the red and green. This distance is shorter than the 10 m pixel size, but comparable to the requirement for co-registration of the MSI sensor set to 3 m for 3 standard deviations (Drusch et al., 2012). In other words, Sentinel-2 can detect wave motions, but is the instrument and processing accurate enough to detect the generally smaller variations in phase speed associated with currents? In fact, Figure 3 shows that the phase speeds down to 25 m wavelength are consistent with linear wave theory but large fluctuations of the order of 1 m/s are found

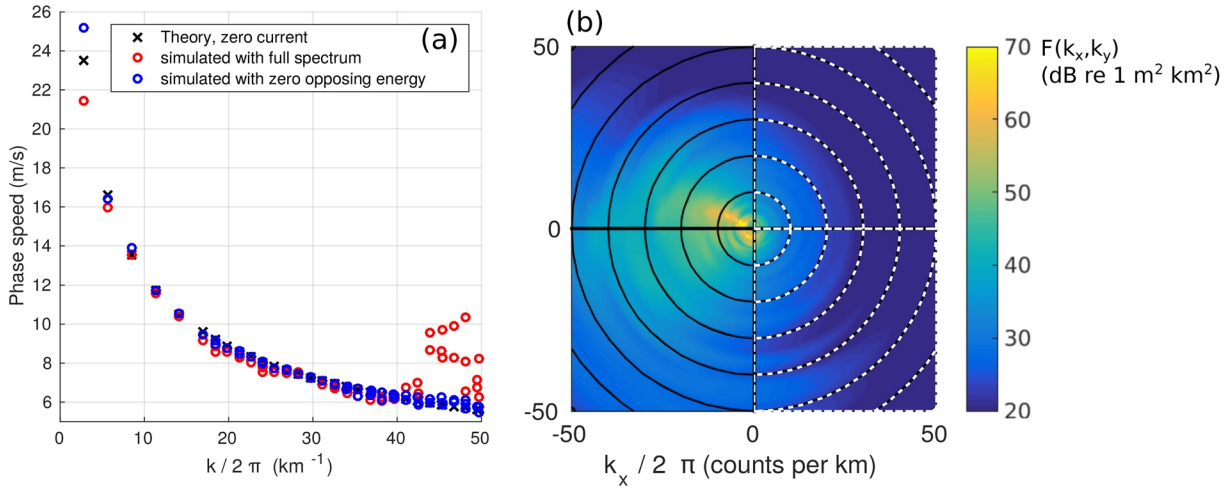

Figure 4. (a) Phase speeds for the simulated image in which either the full spectrum $F(k_x, k_y)$ is taken or the right half of the spectrum $F(k_x \geq 0, k_y)$ is set to zero to have zero opposing wave energy, for directions $130° \leq \varphi \leq 140°$. (b) Wave spectrum estimated from buoy data and used in the simulation, energy is represented in the direction from which waves are coming, that is, corresponding to negative frequencies.

between 25 and 20 m wavelengths, and these vary strongly with the choice of azimuth φ. Such fluctuations are not included in the surface current estimates made by Yurovskaya et al. (2019), because these authors exclude spectral components with a coherence under 0.8. This coherence, denoted "coh" in the following equations and figures, is also called magnitude-squared coherence. We note that this threshold is equivalent to a standard deviation of the co-spectrum phase ψ of 40°, because for small values of the phase ψ in radians, $\text{std}(\psi) \simeq 2\sqrt{1 - \text{coh}}$.

If the vertical shear in the top few meters is to be measured, we have to use these shorter wave components. Presumably, we could use spectral components with a lower coherence, hence a larger uncertainty, and use the averaging over a larger number of spectral components to mitigate this larger uncertainty. For the shorter components, with $k \simeq 40$ cpkm, the coherence is under 0.35 for all directions, and highest for $110° < \varphi < 120°$, with a corresponding fluctuation of the phase $\text{std}(\psi) \simeq 70°$. Interestingly, the same low coherence and high level of phase fluctuations are also present in the simulated data, even when the noise level is reduced to zero. We found that this pattern was not associated to the amplitude nor to the additive or multiplicative nature of the noise in Equation A1, nor even the nonlinear modulation transfer function. The low coherence persists as long as some energy remains for waves in opposing directions.

These fluctuations in the phase speed for the shortest wave components disappear in the simulation when the input spectrum is "chopped" to remove waves propagating from the east (with $k_x < 0$, see Figure 4). Clearly, the spurious large values of phase speeds for wavelengths $20 < L < 25$ m are associated with a significant level of energy in opposing directions.

Any spectral component (k, φ) contains information that propagates in both directions φ and $\varphi + \pi$. By interpreting the phase difference $\psi_{1,2}$ as the phase of a single traveling wave, in direction φ if the phase speed is positive, we are assuming that we can neglect the waves in the opposite direction. In fact, the data is in general the sum of two wave trains traveling in these opposite directions, each giving a different contribution to the phase difference $\psi_{1,2}$, one of these two can be neglected if its energy is much weaker (typically with a difference of 20 dB or so), which is not the case in our example for $L < 25$ m. The magnitude of wave energy in opposing directions for wavelengths under 20 m has been particularly studied for the retrieval of surface wind direction using HF radar (e.g., Kirincich, 2016), but few studies have been performed for longer wavelengths (Tyler et al., 1974).

To quantify the magnitude of waves in opposing directions, we define an "opposition spectrum,"

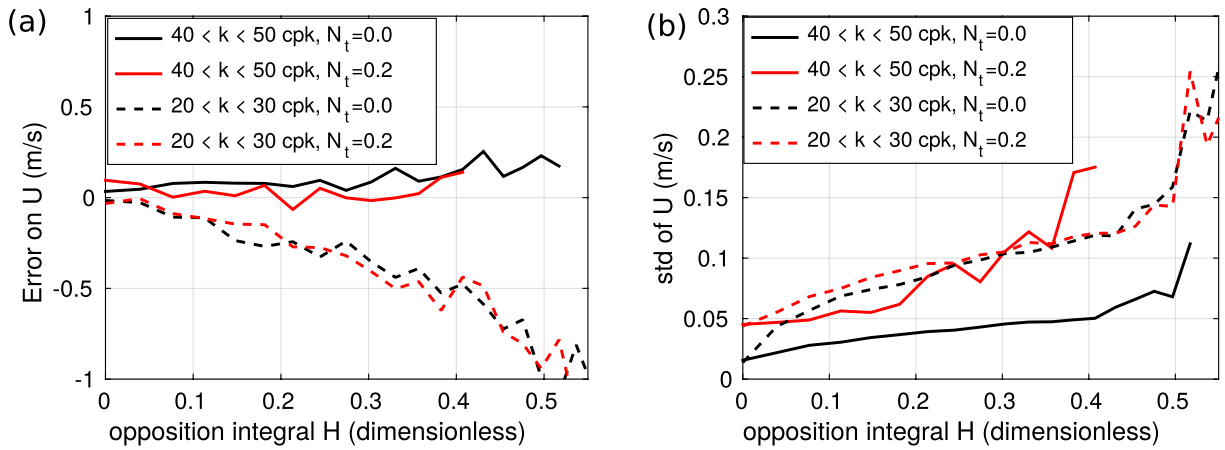

Figure 5. Errors in current retrieval for directions $110° < \varphi < 120°$ as a function of the opposition spectrum H using the same simulated spectrum as in Figure 4. (a) Mean current value (and thus error since the input current is zero) (b) standard deviation of the current.

$$H(k,\varphi) = \frac{4E(k,\varphi)E(k,\varphi+\pi)}{\left[E(k,\varphi)+E(k,\varphi+\pi)\right]^2}. \tag{5}$$

As defined, H ranges from 0 for waves propagating only in direction φ, to 1 for equal amplitudes in opposing directions φ and $\varphi+\pi$. This is the directionally distributed counterpart of the "overlap integral" $I(k)$ defined by Farrell and Munk (2008). $I(k)$ was first used by Hasselmann (1963) and Brekhovskikh et al. (1973) for the theory of generation of secondary microseisms and microbaroms (see Ardhuin et al., 2015; De Carlo et al., 2020, for recent reviews). If $H(k, \varphi)$ is independent of φ then $I(k) = H(k, \varphi)$.

Starting from the same wave spectrum as in Figure 4, we have simulated images with different noise levels N_t and replaced the spectral level in the left-propagating components ($0° < \varphi < 180°$) with values given by a constant r times the values at $\varphi+\pi$, giving a constant $H = 4r/(r+1)^2$. The result of these academic tests is shown in Figure 5. Looking at the mean error for the current U and the standard deviation of the value of U, it is clear that a larger opposition spectrum gives a larger error. Part of the larger error comes from a larger number of spectral bins for which the standard deviation of the cross-spectral phase is larger than 60° and is thus not included in the average. That effect also explains why no value is shown for $N_t = 0.2$ and $H > 0.41$: all spectral bins in that case had a std(ψ) > 60°. Even for $N_t = 0$, the presence of opposing waves leads to very large biases on U that cannot be detected by inspecting only std(ψ). In other words, it may not be feasible to flag errors caused by the presence of waves in opposing directions when using the co-spectrum phase to estimate the surface current. For the case shown in Figure 5a, the error can be up to 0.25 m/s for $H = 0.2$, which would be the value given right off the coast by a 5% coastal reflection, which is a typical value for steep beaches or rocky shores (Ardhuin & Roland, 2012). These results are very robust and do not change qualitatively when changing the shape of the wave spectrum. We suspect that the general larger errors for smaller wavenumbers are associated with the smaller phase shift of the longer waves, corresponding to a lower signal-to-noise ratio.

2.2. Coastal Reflections and Longer Wave Components

We may look for further evidence for the effect of waves in opposing directions by looking at recent images acquired off the Oahu north shore, Hawaii on May 23, 2020, as shown in Figure 6. Error bars on the phase speeds in Figures 7b, 7d, 7f and 7h correspond to ±1 standard deviation of the phase speed, divided by the square root of the number of independent spectral estimates, giving an uncertainty on the average assuming a Gaussian distribution.

Previous study by Ardhuin and Roland (2012) has found evidence of significant coastal reflection, with an energy reflection coefficient of the order of 10%, that would give $H \simeq 0.3$ right at the shoreline, a value that

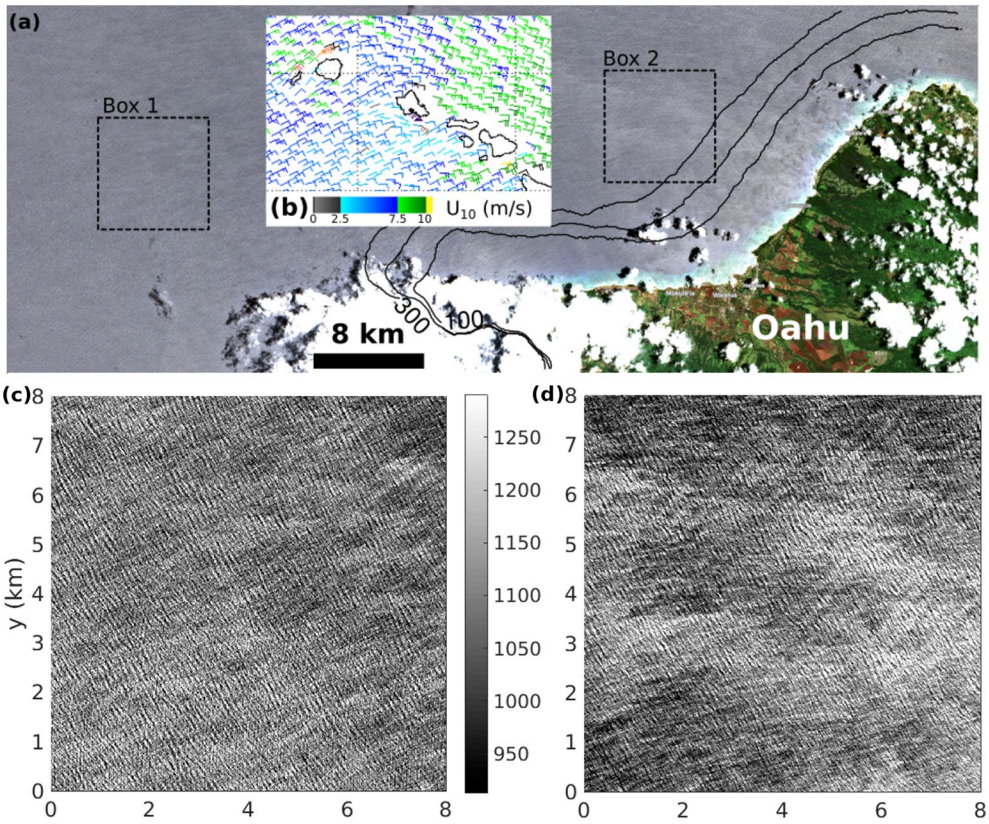

Figure 6. Sentinel-2 image off the North Shore of Oahu. (a) True color image and location of analysis boxes 1 and 2. (b) Wind speed and direction from ASCAT. (c and d) are the channel B04 values for Box 1 and Box 2, respectively.

decreases away from the shore as the reflected part of the wave spectrum is broadened by the variability of the shoreline direction and refraction. Numerical simulations of the sea state typically give $H < 0.1$ in Box 2. As a result, the effect of shoreline reflection is rather weak.

Looking at the dispersion of 250–300 m wavelengths from the North-West, there is a narrow spectral peak (Figure 7a) with phase speeds ranging from 10 to 20 m/s (Figure 7b). However, Box 2 has very similar noise levels and phase speeds. In both cases, the estimated phase speed is very far from the linear phase speed, and the O(5 m/s) difference cannot be reasonably attributed to the current. Our interpretation is that the phase difference between the B04 and B02 images is biased low because some of the estimates are dominated by noise, even though our coherent sum of the co-spectra was weighted by the spectral energy. In this case, the strongest spectral component in (Figure 7e) with $k_x = 2.5$ cpkm and $k_y = -2.5$ cpkm is the one with the largest velocity magnitude (17 m/s) in (Figure 7f), but the random distribution of phases gives an uncertainty of ±3 m/s, and the coherence is 0.94.

Looking at the full spectrum, we find that all the velocities are also probably biased by an error in the relative position (co-registration error) of the two bands B04 and B02, and/or an error in the time lag. Whereas the given geometry of the measurements gives a time lag of 1.00 s, it would take a roughly 1.0 m/s current in azimuths $20° < \varphi < 80°$ to explain the measured phase speeds for k in the range 30–40 cpkm, and the estimated current should vary like $\cos(\varphi - \varphi_U)$. Instead, the observed wave dispersion is more consistent with a time lag of 0.87 s and a much weaker current. That time lag difference of 0.13 s, with a phase speed of 7 m/s is also equivalent to a bias of 0.9 m in the location of the pixels, that could be caused by a bias of 1 microradian in the knowledge of the relative pointing of the different bands for the same detector. We also note that the 1 m/s order of magnitude of the possible error on the current velocity is consistent with the spurious stripes appearing in maps of surface current estimated by Yurovskaya et al. (2019) and O(1 m) co-registration errors found by Kääb et al. (2016).

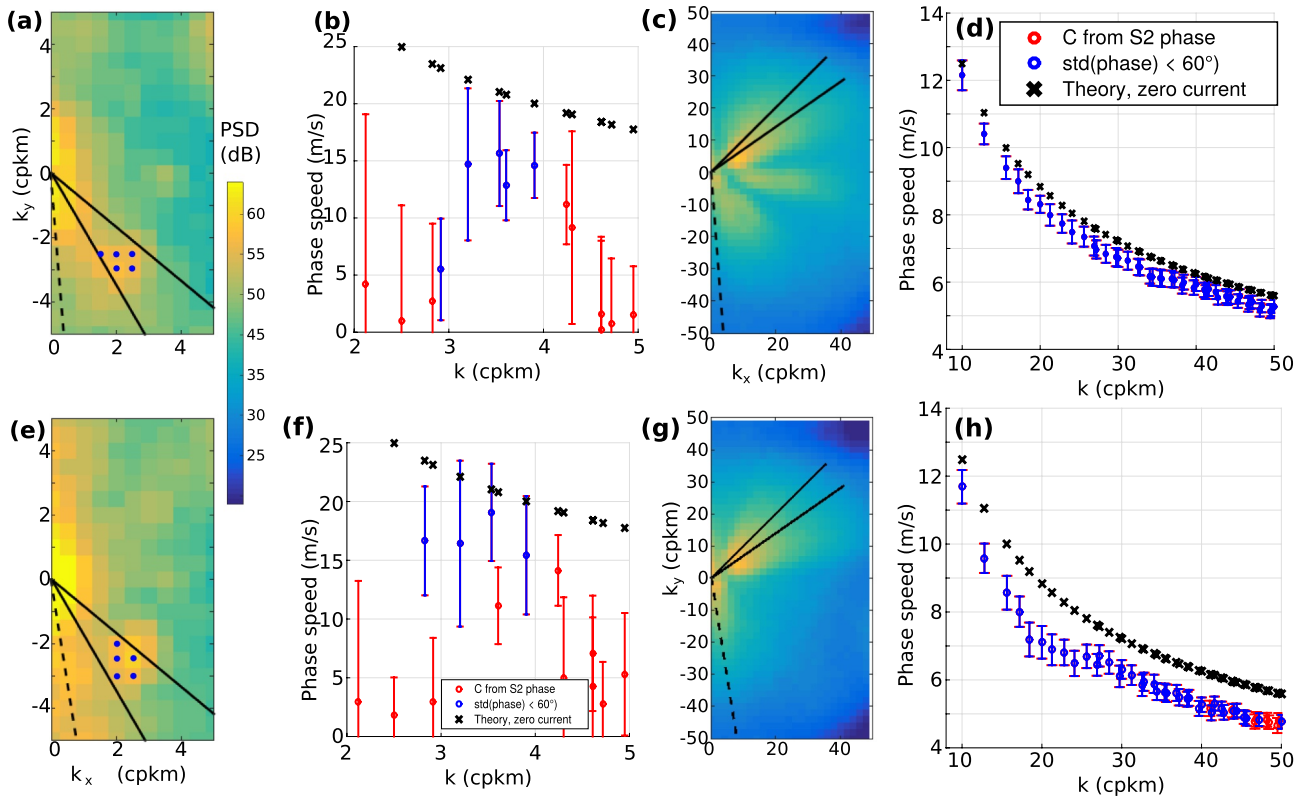

Figure 7. Analysis of two pieces of the S2 image shown in Figure 6. For Box 1, (a) shows the power spectral density of the image intensity obtained with 2 km by 2 km tiles to give a better spectral resolution for wavelengths around 300 m, with dots marking the "low noise spectral components" that give a standard deviation of the co-spectrum phase under 60° and (b) the phase speed of long wave components with directions between 130° and 150°, with blue bars corresponding to those low noise spectral components. (c and d) were obtained with 500 m by 500 m tiles focusing on shorter waves with directions between 45° and 55°. (e–h) show the same quantities for Box 2. The dashed lines in panels (a, c, e, and g) indicate the blind azimuth (see Figure 2 for its definition) and the blue dots in (a and e) indicate the spectral components for which the std (phase) is less than 60°, with velocity estimates shown with blue symbols in (b and f).

More interestingly for the purpose of the present study, the variation of phase speed as a function of wavenumber has an O(50 cm/s) anomaly in Box 2 for k around 20 cpkm. Could that be the signature of a current maximum at a depth around 10 m? In the absence of verifying measurements, we cannot explore this with any certainty.

3. Least Squares Method Applied to a Sequence of Three Images

Going back to the problem of estimating phase speeds for the shorter wave components that often have relatively large values of H, we propose to try to separate the waves in opposing directions, and for this, use more than two images. This problem is very similar to the problem of separating waves in opposing directions in wave laboratory experiment, which is necessary for implementing absorbing boundary conditions at paddle wave makers. The founding paper in this line of work was the method of Mansard and Funke (1980) for computing wave reflection using a series of three wave gauges with a least squares method. It was later improved on by Zelt and Skjelbreia (1993). We are not aware of an adaptation to image processing and generalization of the method to estimate currents at the same time as the amplitudes of the two opposing wave trains. As detailed in Appendix B, this generalization is straightforward.

We first tested the method for simulated monochromatic waves of 50 m wavelength propagating in one dimension and resolved at $dx = 10$ m resolution with time lags of 0.5 and 1.0 s similar to the red, green, and blue bands (B04, B03, and B02) of Sentinel-2. We found that adding one extra measurement at a 0.8 s lag, similar to band B08 on Sentinel-2, had a limited impact on the results. The method is illustrated in Figure 8 with spatial series, with or without noise.

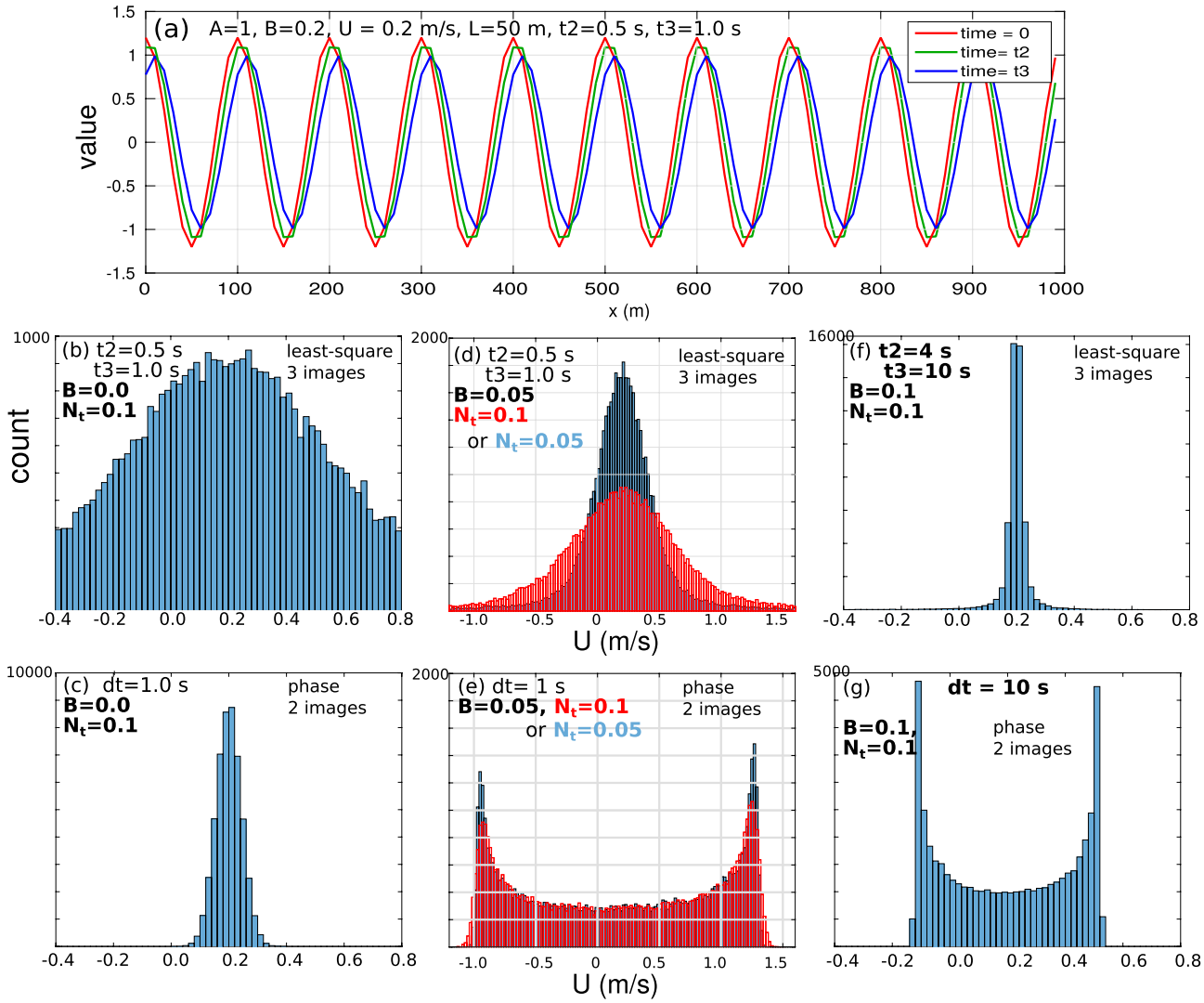

Figure 8. (a) Example of three spatial series at three different times in the presence of rightward propagating and leftward propagating waves of wavelength $L = 50$ m, amplitudes $A = 1$ and $B = 0.2$, and a $U = 0.2$ m/s current. The time lags of 0.5 and 1 s are typical of Sentinel-2 data for the 10 m resolution R, G, and B channels. (b–g) Monte Carlo simulations of the estimation of the current velocity U from 50,000 monochromatic spatial series with white multiplicative noise of amplitude N_t, using least squares in (b, d, f), and using the phase difference between two images in (c, e, g). For reference, the distribution of estimated currents is also shown in (b, c) when the amplitude of leftward propagating waves is zero.

With a small value of the opposition spectrum, here $A = 1$, $B = 0.1$ and thus $H \simeq 0.04$ (except for $B = 0.2$ in Figure 8a), the wave field looks like a single propagating wave with a modulated amplitude, changing from 1.1 to 0.9 over half a wave period, here 2.8 s, due to the partial standing wave. When multiplicative noise is added, the distribution of current estimates from phase differences is Gaussian for waves propagating in only one direction (Figure 8c). In the case of the least squares method, the distribution has heavier tails than a Gaussian distribution and thus requires a very broad range of velocities to be properly characterized. In our example, the uncertainty is 20 times larger when using the least squares method (see Figure 8b compared to Figure 8c). In contrast to A and B, we do not have an analytical expression for U and it is difficult to predict its distribution. In practice, we find that the median of the distribution of U is apparently not biased (Figure 8b, 8d and 8f), and the mean of M estimates of this median apparently converges following the central limit theorem with a standard deviation reduced by $1 / \sqrt{M}$. One may thus hope to retrieve the current with this method, even for noisy data.

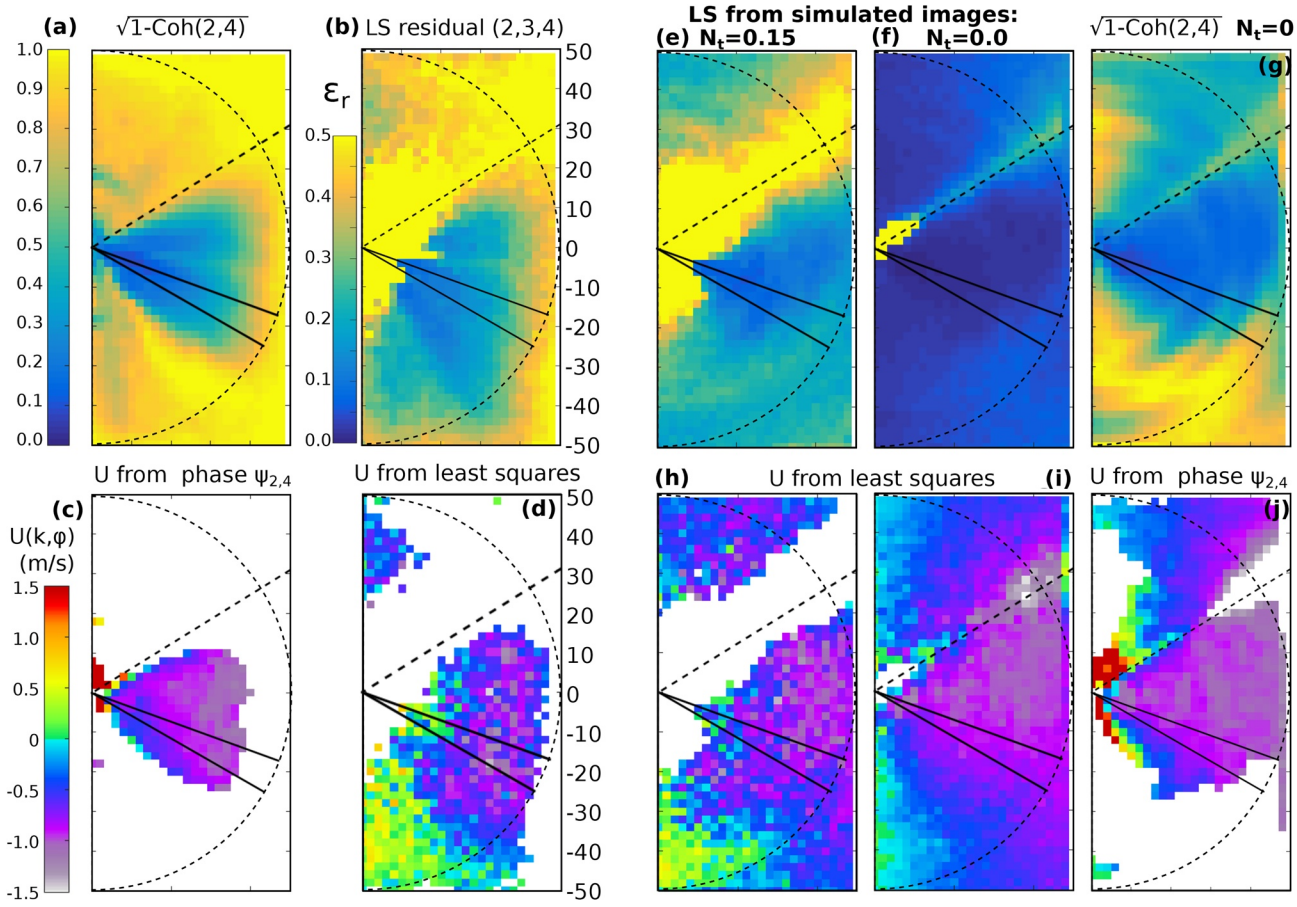

Figure 9. All the panels show quantities in spectral space ($0 < k_x < 50$ cpkm, $-50 < k_y < 50$ cpkm). Top panels (a, b, e, f, g): Error metric (coherence for phase method, standard deviation of normalized residual for least squares method). Middle panel (c, d, h, i, j): Estimate of velocity in φ direction. The dashed circle corresponds to $k = 50$ cycles per km. The simulated images include a non-zero current vector $\mathbf{U} = (-1, 0)$ m/s, so that the current component in direction φ should be $-\sin(\varphi)$, very close to what is retrieved in panel (i).

We note that the uncertainty on the current U, as measured by the standard deviation of the distribution of U, is not affected by the presence of waves in both directions when using the least squares method: changing the value of B from 0 (Figure 8b) or 0.05 (Figure 8d) to 0.1 has no influence on the distribution (not shown). With the least squares method, the current uncertainty generally decreases when reducing the noise (Figure 8d) or increasing the signal, for example, when increasing the time differences between the measurements (Figure 8f). In contrast, when waves in opposing directions are present, the error reduction in the phase method is very limited when the noise is reduced (Figure 8e). Both methods are improved when the time lag is increased by a factor 10, as shown in Figures 8f and 8g.

We now apply the least squares method to actual Sentinel-2 imagery, with three bands (B02, B03, and B04). We first note that the image amplitude and standard deviations are different for the different bands, so that the shift from one band to another is not just a propagation but also includes a change in mean value and amplitude. To mitigate the effect, we have shifted and rescaled the pixel values so that each image has a zero mean and unit standard deviation before computing Fourier transforms.

We first take up our example off California, with results shown in Figure 9. Noisy parts of the spectrum generally correspond to a low coherence in image pair (Figure 9a) and a high uncertainty for the co-spectrum phase (already shown in Figure 3) and hence current velocity. When using a least squares fit, an obvious candidate for quantifying the noise is the residuals that we have normalized by the sum of the spectral densities of the images.

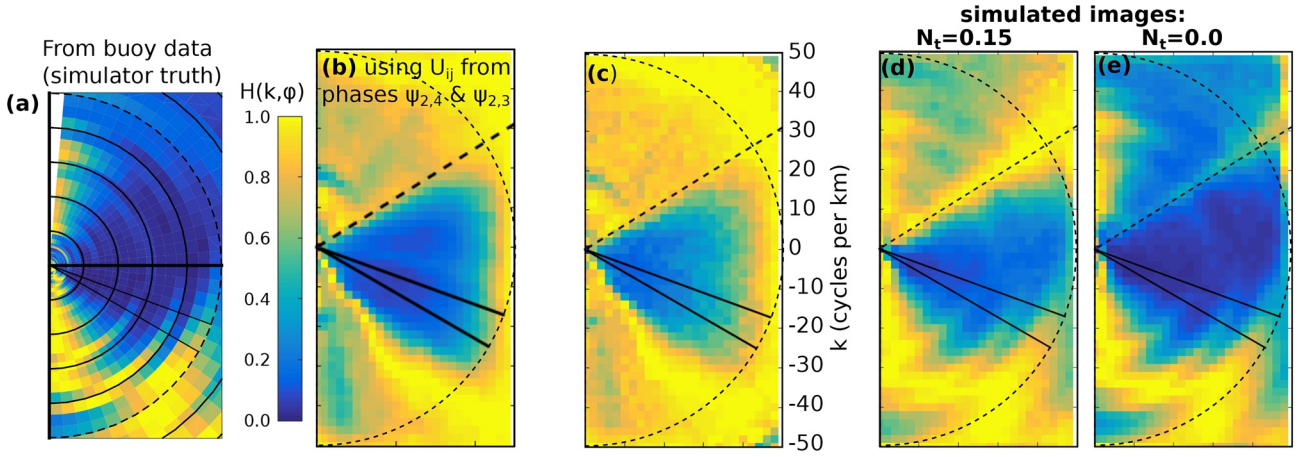

Figure 10. Estimates of the opposition spectrum $H(k, \varphi)$, for the spectral range ($0 < k_x < 50$ cpkm, $-50 < k_y < 50$ cpkm). Panel (a) shows the H spectrum based on the MEM-estimated spectrum from the in situ buoy, (b and c) show two estimates from the Sentinel-2 image using either the current estimated from phase differences or the current also given by the least squares method. (d and e) are the results for simulated images with different levels of noise.

For each spectral component (k, φ) and each m-index subimage of 100 by 100 pixels we fit the amplitudes $Z_{A,m}(k, \varphi)$ of a wave train traveling in direction φ and $Z_{B,m}(k, \varphi)$ traveling in direction $\varphi + \pi$ and the current velocity $U_m(k, \varphi)$ that minimizes the sum of square residuals that is the difference between the image spectral density $B_{n,m}(k, \varphi)$ and our model of two counter-propagating components (see Appendix B). We only keep values of U that fall in the range from -5 to 5 m/s, for which there is a number $M(k, \varphi)$ of estimates. For each spectral tile we have a normalized residual,

$$\varepsilon_m(k,\varphi) = \sqrt{\sum_n \left|\varepsilon_n(k,\varphi)\right|^2 \Big/ \sum_n \left|B_n(k,\varphi)\right|^2}. \tag{6}$$

From these "successful fits," their number is $M(k, \varphi)$, we take the current to be the median of the $U_m(k, \varphi)$ values and we define a root mean square residual,

$$\varepsilon_r(k,\varphi) = \sqrt{\sum_m \varepsilon_m^2 \,/\, M(k,\varphi)}. \tag{7}$$

Inspecting (Figure 9b), we propose that a first not-too-conservative but reasonable threshold for acceptable results is $\varepsilon_r < 0.4$, giving the current values shown in Figure 9d. This choice was motivated by the desire to include the spectral components for which we found that waves in the opposite direction were a significant source of error for the phase method, but this also keeps spectral components with very low signals (with azimuth directions between 0° and 30°, and between 135° and 180°).

In addition to the current, we also estimate the opposition spectrum as

$$H(k,\varphi) = \frac{4 \mid Z_A \mid^2 (k,\varphi) \mid Z_B \mid^2 (k,\varphi)}{(\mid Z_A \mid^2 (k,\varphi) + \mid Z_B \mid^2 (k,\varphi))^2}. \tag{8}$$

Although we have no direct measurement of the true directional spectrum $E(k, \varphi)$ and thus of $H(k, \varphi)$ using Equation 5, we may compare estimates H_i to the values shown in Figure 10a and given by the wave spectrum estimate $E(k, \varphi)$ using the maximum entropy method (MEM), which is used in the image simulations. It is not clear at all if the MEM derived spectra give values of $H(k, \varphi)$ that should have the same order of magnitude as those given true directional spectrum. This question could be investigated with stereo-video data (e.g., Guimarães et al., 2020).

When using the least squares estimate of Z_A and Z_B that correspond to the least squares estimate of U for each image tile, the values recovered from the S2 image are typically much higher than those estimated from the buoy as shown in Figure 10a): in the range 0.2–0.4 for the part of the spectrum that has a coherence

squared higher than 0.64 which is already lower than the 0.8 threshold in Yurovskaya et al. (2019). This value of H is probably at least 10 times too high around the spectral peak. These would typically give a background level of microseism sources that is too large by a factor 10 or more. What happens is that the fitting procedure puts some of the noise in the amplitude of the opposing waves. As a result, a lower threshold than $\varepsilon_r < 0.4$ is necessary to give accurate estimates of the opposition spectrum H. But we can also force the current to the value estimated from the phase method and only fit Z_A and Z_B, in that case, the values of H are more realistic, as shown in Figure 10b.

For that estimate, we have also modified the equations in Appendix B to allow for a different current at times t_2 and t_3 to absorb the biases in the image position $(\delta X,\delta Y)_{i,j} = (U_{ij}, V_{ij}) \times (t_j - t_i)$. Indeed the phase difference $\psi_{2,3}$ gives a velocity vector close to (−1.8,0.) while $\psi_{2,4}$ gives (−1,0) corresponding to a 1 m eastward erroneous shift of the B02 image relative to B03 and B04. This inconsistency in the data is not included in the fitted model proposed in Appendix B and thus contributes to higher errors in the estimate of U. One possibility may be to recompute the least squares with different velocities over the different time lags, or to use the phase difference method on all image pairs to estimate deviations from a constant speed and shift the image before applying the least squares method.

For our test image, it is thus dubious that the least squares method, as implemented here, has provided any additional reliable information for short waves compared to the phase method. Using a more conservative threshold $\varepsilon_r < 0.2$, it is possibly able to slightly extend the part of the spectral plane from which a velocity can be derived to directions that are further away from the mean wave direction.

Looking beyond the particular case of the bands B02, B03, and B04 of the Sentinel-2 sensor, it is interesting to know how well this method may work. We have thus simulated the image and its processing, and reduced the noise level from $N_t = 0.15$ (which looks similar to the true Sentinel-2 image) to no noise at all with $N_t = 0$. Without any noise, the least squares fit is very good with $\varepsilon_r < 0.1$ for the full spectral domain, except around the blind azimuth. As a result, the input current vector $\mathbf{U} = (-1, 0)$ m/s is very well recovered. This would not be the case for the shortest components using the phase method except in the mean direction, giving only one component of the current vector.

The precision on the retrieval of the surface current is further illustrated in Figure 11, focusing on a narrow range of azimuths, between 110° and 120°. The error bars give an estimate of the precision of the mean within each spectral bin that are all completely independent. For the phase-difference method, the smooth variation of the estimates across the spectra (within the error bar) confirms that the O(15 cm/s) precision for each spectrum estimate is realistic. This does not say anything about the accuracy of the estimate that is dominated by an O(1 m/s) error due to relative pixel co-registration errors of the different bands.

For the least squares method, the error bars are more difficult to define given the heavy tails of the U distribution and the sample size (256 independent spectra giving 256 estimates of U). It might be possible to use the distribution of residuals ε_m obtained for the M spectra as given by Equation 6, because they are correlated with errors on U, but we have not found a satisfactory parameterization that would work for both the academic 1D case of Figure 8 and the true images. If needed, the only robust uncertainty we can propose is to compute the standard deviation across neighboring spectral components, for example, in a 10 cpkm band of wavenumbers.

Both the phase and least squares method agree in the range 25–35 cpkm, but there are large biases of the least squares method for both short and long components, as shown in Figure 11a. Although some of these errors could be caused by instrument errors (such as errors in the retrieved observation angles that could change the estimate time lags and distort the dispersion relation), it is striking that the simulated data shown in Figure 11b gives similar errors, but slightly weaker, which leads us to think that the biases in the least squares method may be dominated by artifacts of the processing method. We have not yet identified the source of these errors. We also note that the phase method, in contrast, has no trend in the simulated data for which the standard deviation of the phase is under 60°.

We generally expect that errors can be reduced by increasing the time separation of the images so that the mean phase difference is much larger, making random phase differences comparatively smaller. Figures 11c and 11d show that realistically noisy images with a doubled time lag are preferable to a noise-free

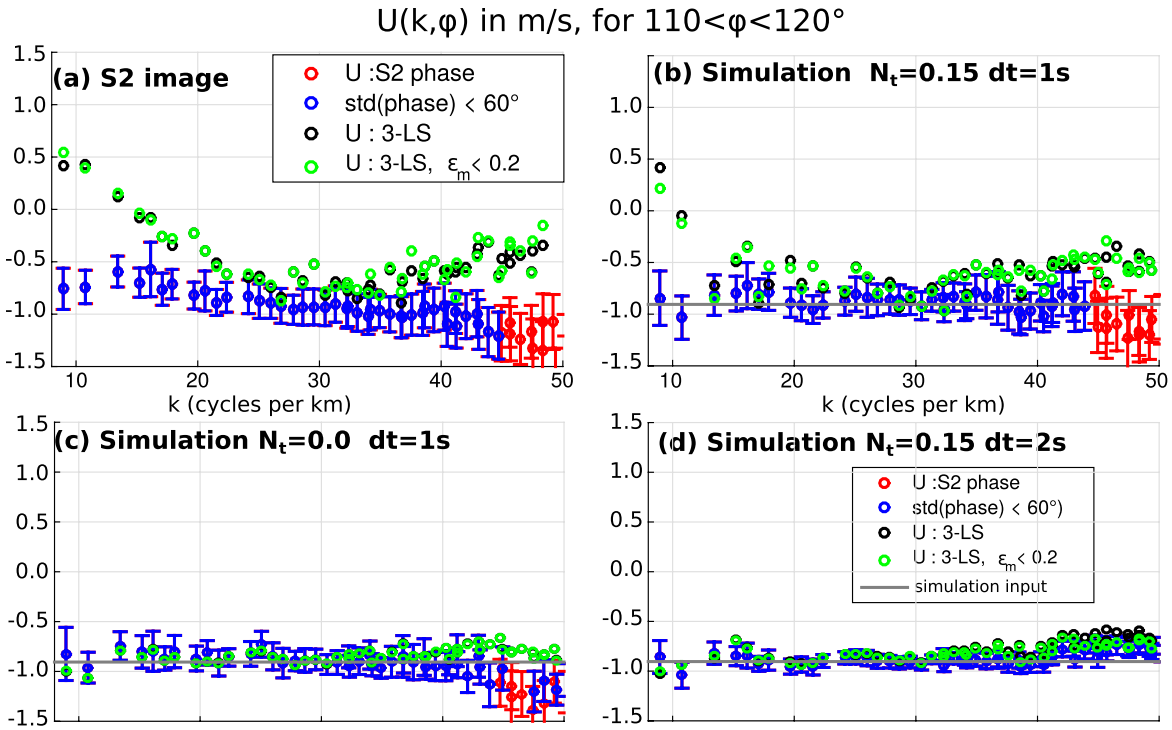

Figure 11. Comparison of different current estimates for waves in azimuths 110°–120° for (a) Sentinel-2 data using bands B04, B03, and B02, and simulated data with the (b) same time lag and similar noise level, or (c) no noise, or (d) a doubled time lag. For the phase difference method (red and blue symbols), the error bars show the mean value obtained for each spectral component plus or minus one standard deviation divided by the square root of the number of estimates. We have also tested (in green) using a subsample of the least squares, keeping only those with small values of the residual ε_m.

image with the same time lag. This is easy to understand in the case of the phase difference method: the larger phase difference makes the random-phase noise a relatively smaller term in the phase difference. The uncertainty on U is inversely proportional to the time difference.

The first verification of this advantage of larger time lags is provided by using the B12 and B11 band, that are acquired 1.1 and 0.5 s before B04, which is here 1 s before B02 (this ordering correspond to the even detectors on S2, it is reversed for the odd detectors). Hence combing B12 with B11 and B02, giving a maximum time lag of 2.1 s. Because the spatial resolution of B12 is only 20 m, we have averaged B02 over 2 by 2 pixel boxes to provide images at the same resolution, including a 1 m westward shift of B02 to correct for the error noted above. These results are illustrated in Figure 12.

We first note that the shape of the spectrum, here resolved at higher spectral resolution, shows a 3-lobe structure with minima of the image power spectral density and coherence for the azimuths 100° and 125°, these are probably due to artifacts of the Level 1-C processing. For the waves in the direction of highest coherence, $108° < \varphi < 118°$, the uncertainty on U obtained in the range of wavenumbers 10–20 cpkm is as low as 0.1 m/s in spite of the average of only 64 independent tiles (compared to 256 for Figure 11a). Combining all the 25 spectral components available from 10 to 20 cpkm gives an uncertainty of 3.4 cm/s, which we estimated from the mean of the uncertainties divided by the square root of the number of spectral components. Performing the same analysis on 20 m box averages of B03 and B02 gives a 5.8 cm/s uncertainty. It is therefore beneficial to use the largest time lags for estimating the current speed from wavelength between 50 and 100 m. We note that the least squares method gives rather puzzling results that we do not understand, with a variation of the estimated current as a function of wavenumber that is large and not random.

In the case of the waves shorter than 40 m wavelength, that are only resolved in the 10 m images such as given with bands B02 and B04 with 1 s time lag, the uncertainty of U from the phase difference method for wavenumbers from 30 to 40 cpkm is larger at 4.8 cm/s due to the opposing effects of a lower coherence and a larger number of spectral estimates.

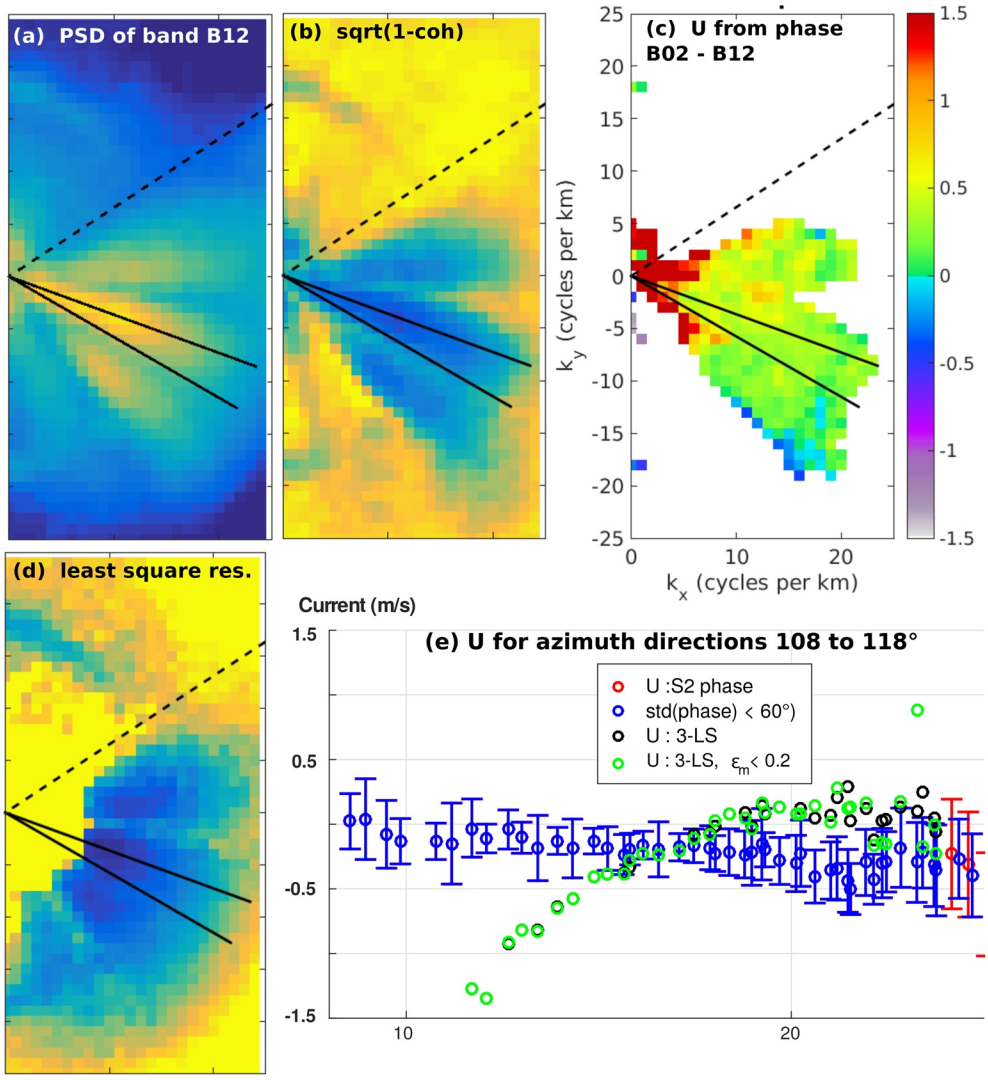

Figure 12. Example of results with a larger time lag of 2.1 s but coarser ($dx = 20$ m) using B12 and B02 bands. To better resolve the longer waves, the spectral analysis was done here with 1 km by 1 km tiles.

4. Discussion: Consequences for Surface Current Velocity and Shear Retrieval

4.1. Application to Sentinel-2

From the consistency of the velocity estimates for all spectral components, and in the particular case of the image analyzed in Figures 2 and 11, we find that Sentinel-2 imagery is capable of providing a velocity precision of the order of 5 cm/s for spectral ranges of 10 cycles per kilometer. These uncertainties are of the order of the differences in the advection speed of the different spectral components due to a typical vertical current shear in the top 20 m of the ocean. Along the equator with differences of the order of 50 cm/s between can be found between 1 and 15 m depth and these should be detectable by Sentinel-2. A probably more typical shear, from subtropical Atlantic measurements, is shown in Figure 13 and measuring it requires detecting 3 cm/s differences between $k = 20$ and $k = 40$ cpkm. Resolving this demands a reduction of the uncertainty by at least a factor 3, possibly obtained by averaging over at least 24 by 24 km.

At that level of accuracy, other phenomena may be involved, such as nonlinear wave effects, that include both an advection of short waves by long waves (Broche et al., 1983; Weber & Barrick, 1977) which corresponds to a fraction of the Stokes drift (Ardhuin et al., 2009), and the presence of harmonics (i.e., Leckler et al., 2015). To test that latter effect, we have made some simulations by replacing the linear wave model

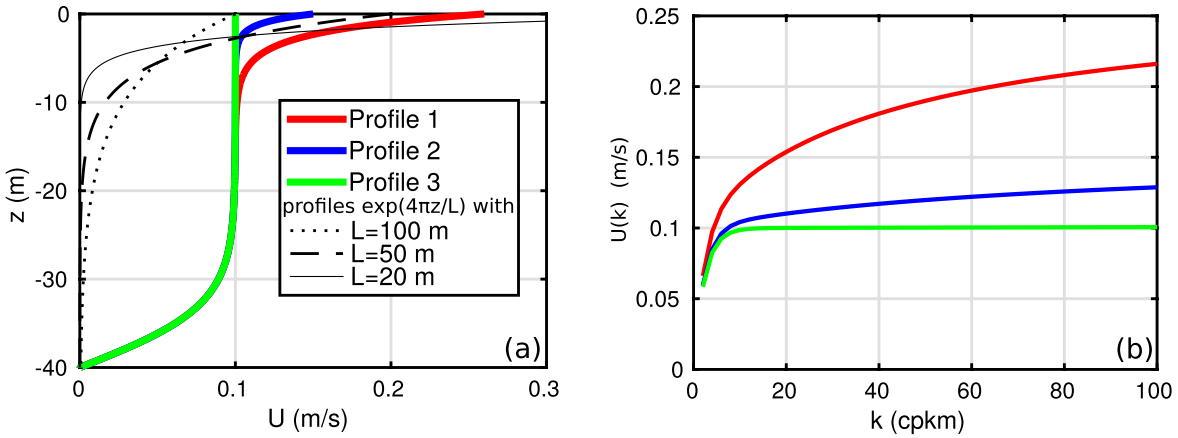

Figure 13. (a) Example of typical current profiles of summertime subtropical gyres. Profiles 1 and 2 correspond to Figure 1, while profile 3 would be a hypothetical total current profile without Stokes drift. (b) Resulting variation of the effective current U(k) as a function of the wavenumber.

with the Choppy Wave Model (Nouguier et al., 2009), which is a first-order Lagrangian theory. We use a current ($U_x = -1$ m/s, $U_y = 0$.) in our simulations.

Following (Yurovskaya et al., 2019), we estimate U_x and U_y by a least squares fit to the measured phase differences after removing the linear wave dispersion,

$$\psi_a(k_x,k_y) = \left(\psi(k_x,k_y) - dt\sqrt{g\sqrt{k_x^2+k_y^2}}\right) / \, dt \tag{9}$$

which is related to the current vector (U_x, U_y) by

$$\psi_a(k_x,k_y) = k_x U_x + k_y U_y + \varepsilon(k_x,k_y), \tag{10}$$

where ε is a small residual. We only keep the M spectral components with index m corresponding to one pair (k_x, k_y) such that $|k_m| > 10$ cpkm, $|k_m| < 40$ cpkm and with std(ψ) < 60°. This gives a length M vector $Y = (\psi_{a,m})_{1\le m\le M}$. We invert Equation 10 for all m to find the vector $X = (U_x, U_y)$ that gives the smallest sum of square residuals weighted by $1/\text{std}(\psi)^2$. The resulting uncertainty σ_U is the square root of the first term of the matrix $(A'CA)^{-1}$ where $A(m, 1) = k_{x,m}$, $A(m, 2) = k_{y,m}$ and C is the diagonal matrix such that $C(m,m) = 1 / \text{std}(\psi_m)^2$ (Hogg et al., 2010).

In our case, we take as a reference $\sigma_{U,I} = 0.018$ m/s the uncertainty on retrieved U for the case of a linear MTF and linear surface. This uncertainty is not zero due to all the processing steps: use of subimages, windows, and so on. Presumably the effect of non-linearities or waves in opposing directions are independent from these processing effects and we estimate the excess uncertainty due to effect Z, as

$$\sigma_{U,Z} = \sqrt{\sigma_U^2 - \sigma_{U,I}^2}. \tag{11}$$

The retrieved current and excess uncertainty are reported in Table 1 for four different simulations.

We find that the effects of nonlinearities introduced by the Choppy Wave Model for wavelengths larger than 20 m and in the case considered here, are comparable to the effect of the nonlinear MTF and nine times smaller than the effect of waves in opposite directions. Possibly nonlinearity becomes more important when waves much shorter than $L = 20$ m are taken into account.

Table 1
Effect of Nonlinearities and Opposing Waves on Retrieved Current

Simulation	U value	$\sigma_{u,Z}$
Linear model	−0.974	0.000
Choppy wave model	−0.976	0.011
Nonlinear MTF	−0.975	0.004
Opposing waves	−0.899	0.107

Also, waves are not homogeneous in space, with gradient driven by the horizontal shear of small-scale currents (Ardhuin et al., 2017; Quilfen & Chapron, 2019; Villas Bôas et al., 2020). If the shorter waves correlate with currents in a way different from the longer waves, which can be the case at the smallest scales (Suzuki, 2019), what appears like a vertical shear in the difference of phase speed could be the effect of the horizontal shear. Detailed simulations of these effects will be needed to find the order of magnitude of horizontal shear contributions to the mean phase speed difference.

In general, the vertical shear of the current is a priori not sensitive to image co-registration errors because all wavelengths are affected by these errors in the same way, and the shear is associated by a difference in phase speed of the different wave components. We find that a 10 cm/s difference in phase speed between 50 and 25 m wavelengths ($k = 20$ cpkm and $k = 40$ cpkm) should be detectable with Sentinel-2 using data from an 8 km by 8 km region of the ocean. Such a difference corresponds to a fairly large current shear in the top 10 m of the ocean.

4.2. Beyond Sentinel-2: A Possible STREAM-O Instrument

Resolving weaker and more typical shears would require more sensitive measurements, such as provided with larger time lags and higher spatial resolution. Figure 13b shows that extending the spectrum to 100 cpkm (10 m wavelengths) would double the difference in velocity that can be detected. Such capability will be available with the next generation Sentinel-2. Using these shorter components will probably require methods that are less sensitive to the presence of waves in opposite directions, such as the least squares method proposed here.

Based on the results shown in Section 3, increasing time lags is probably the most important feature needed to obtain more accurate currents using both the phase difference or the least squares method, with or without waves in opposing directions. Due to data downlink constraints and cloud cover, optical monitoring of currents using wave dispersion cannot compete with the possible coverage given by radar systems (Ardhuin et al., 2019). Yet, optical imagery is uniquely capable of providing estimates of vertical current shear, and may provide very useful data for reducing pointing errors. With these two goals in mind, the "ocean Surface Transport kinetic Energy, Air-sea fluxes and Mixing" (STREAM) concept combines a Ka-band Doppler scatterometer radar STREAM-R with a 1,000-km wide radar swath, with a optical system STREAM-O that takes sequences of five ocean images at 5 m resolution with time lags of 1, 4, 9, and 10 s, overlapping over a 10-km wide strip along the orbit. This concept was proposed for the 11th Earth Explorer of the European Space Agency.

In addition to the increased time lag, the STREAM-O design uses a push-frame acquisition system, instead of the push-broom of the MSI sensor on Sentinel-2. Namely, the raw data for one band consists of 2-D images with large overlaps instead of a single line. Such a feature makes on-board averaging possible, increasing the integration time to a value larger than several times the life time of specular points, that is, 10 ms or more. This is clearly not feasible for a pushbroom system in which the duration of acquisition of each pixel is less than the pixel size (10 m) divided by the ground velocity (7 km/s), that is, 1.4 ms. Future work is needed to understand the parameters that control the phase difference noise in optical imagery. It is possible that other parameters are relevant besides the number and life time of specular points. Also, the present study considered images in the sun glint, but several useful applications (in particular for water depth retrieval) have been made with different observation geometries, with different noise characteristics.

5. Conclusions

To retrieve a surface current vector and current shear from observed wave dispersion, it is necessary to obtain separate and robust estimates of the phase speed of different components of the wave spectrum, with different directions to obtain a current vector, and with different wavelengths that have different sensitivities to different depths.

Although the present study did not demonstrate a full solution method, we have highlighted difficulties associated to the retrieval of phase speed from a small number of ocean surface images using either a phase difference method or a least squares fitting of the current velocity and the amplitude of waves in opposing

directions. Both methods have complementary advantages and should probably be combined and modified for further improvements. We particularly highlighted how the presence of waves in opposite directions causes an error in the phase difference method. In one specific case analyzed here, this is particularly a problem for retrieving phase speeds from waves with wavelengths shorter than four times the dominant wind sea. The least squares method using three or more images is not sensitive to waves in opposing directions, but it provides relatively noisy estimates of the current velocity when applied to Sentinel-2, due to the short time lags (about 1 s). As a result, the least squares method may not provide much more useful additional information on the current velocity than the phase difference method. We also note that anomalously low coherence in image pairs may be an indication of the presence of waves in opposite directions, which may have an application to the identification of strong microseism or microbarom sources.

Our simulations show that when applied to other sensors with lower image noise and/or larger time lags, the least squares method may allow to use the shortest wave components that are more likely to be associated with high levels of energy propagating in opposing directions. We find that a 2 s time separation and the same pixel noise as Sentinel-2 should be sufficient to retrieve reliable phase speeds of shorter waves, all the way to the Nyquist wavelength. In that case, it should be viable to reliably estimate the magnitude of waves in opposing directions as quantified by the opposition spectrum introduced in Section 2. Future work will be needed to refine and verify the error model for the two methods and their possible combination.

Appendix A: Image Simulator

The first five directional moments are converted to a 5-degree resolution directional frequency spectrum using the MEM (Lygre & Krogstad, 1986). This spectrum is then interpolated onto a regular grid in (k_x, k_y) space to obtain power spectral densities of wave-induced surface elevation with a spectral resolution of 1/16,000 cycles per meter, that is, with a largest wavelength of 16 km, two times as large as the region analyzed. Drawing random phases for each spectral component, the wave power spectral density is used to define complex amplitudes that are inverse-Fourier transformed to generate 8 km square grids of the surface elevation and long wave slopes, $\left(s_x(x,y,t_i), s_y(x,y,t_i)\right)$, with x and y regularly discretized at 10 m resolution, and t_i the discrete-time sampling corresponding to the time of image acquisition.

The input to our image simulator are thus

- the wave spectrum $F(f, \theta)$ is transformed to $F(k_x, k_y)$ using linear dispersion with a maximum frequency $f \simeq 0.7$ Hz corresponding to a cut of wavelength of 3.2 m. This spectrum is then interpolated on a regular grid in (k_x, k_y) space, covering the range $[-k_N, k_N]$ for each dimension where k_N is the Nyquist frequency (i.e., corresponding to a 20 m wavelength when simulating 10 m resolution images). This avoids any aliasing;
- the direction of the dominant slopes φ_{mss} (which is generally close to the wind direction);
- the mean square slope in that direction mss_u and the mean square slope in the perpendicular cross-direction mss_c;
- the bistatic view angles β and φ_a for each image (see Figure 2 for a definition), which we assume spatially uniform as we are only representing a small piece of the ocean.

Ideally, a full-wave spectrum including short gravity waves, for example, such as parameterized by Elfouhaily et al. (1997) or extending the model range of WAVEWATCH III to short gravity waves, would also contain the required slope parameters (items 2 and 3 of the above list), but such spectra are not yet realistic enough.

The forward model described in Kudryavtsev et al. (2017a) is used to compute a mean luminance B_0 for a locally rough but flat surface, and the local luminance $B(x, y)$ from the same rough surface tilted by the long wave slopes. Detected luminance fluctuations are caused by the true luminance fluctuations caused by the finite number of specular points that contribute to the signal in each pixel (Longuet-Higgins, 1960).

The image pixel value is then taken as the nearest integer of a mean intensity I times $(1 + n_t)B/B_0$ where n_t is a random white noise of an amplitude N_t that parameterizes the "twinkle" of the sea surface.

The noise of the detector is treated as an additive noise n_d, represented as a Gaussian noise of standard deviation N_d. For each channel j which corresponds to a time t_j we have the pixel value

$$I_j(x,y) = \mathrm{E}(I_j\ B(x,y,t_j)\ /\ B_0(1+n_t)), \tag{A1}$$

where the value E(x) is the largest integer value that is less or equal to x. The quantization effect of rounding to an integer pixel value is not very relevant in the present paper with examples that have a relatively bright sea surface. In contrast, the twinkle noise has a very important influence on the estimation of the surface current, as discussed in Sections 2 and 3.

Appendix B: Adaptation of Three-Probe Least Squares Method to an Unknown Current

Let us have A and B the complex amplitudes of the waves propagating in the φ direction and the opposite direction $\varphi+\pi$, and N is the number of measurements at times t_n. In the case $N=3$, the system of equations for the three measured complex amplitudes F_1, F_2, F_3 at times $t_1=0$, t_2, t_3 is, for each spectral component (k, φ), with U the current component in direction φ, $\sigma=\sqrt{gk}$,

$$A + B - F_1 \quad = \quad \varepsilon_1, \tag{B1}$$

$$A\mathrm{e}^{-\mathrm{i}(\sigma t_2 - kUt_2)} + B\mathrm{e}^{+\mathrm{i}(\sigma t_2 + kUt_2)} - F_2 \quad = \quad \varepsilon_2, \tag{B2}$$

$$A\mathrm{e}^{-\mathrm{i}(\sigma t_3 - kUt_3)} + B\mathrm{e}^{+\mathrm{i}(\sigma t_2 + kUt_2)} - F_3 \quad = \quad \varepsilon_3. \tag{B3}$$

(B4)

We look for the solution that minimizes the sum of the modulus of ε_n squared,

$$\sum_n \left|\varepsilon_n\right|^2 = \sum_n \left(A\mathrm{e}^{-\mathrm{i}(\sigma t_n - kUt_n)} + B\mathrm{e}^{+\mathrm{i}(\sigma t_n + kUt_n)} - F_n\right)\left(\overline{A}\mathrm{e}^{\mathrm{i}\sigma(t_n - kUt_n)} + \overline{B}\mathrm{e}^{-\mathrm{i}(\sigma t_n + kUt_n)} - \overline{F}_n\right) \tag{B5}$$

where the overbar corresponds to the complex conjugate. Taking derivatives with respect to the real and imaginary parts of A and B and taking derivative with respect to U gives, respectively,

$$\sum_n \mathrm{e}^{-\mathrm{i}(\sigma t_n - kUt_n)}\left(A\mathrm{e}^{-\mathrm{i}(\sigma t_n - kUt_n)} + B\mathrm{e}^{+\mathrm{i}(\sigma t_n + kUt_n)} - F_n\right) \quad = 0 \tag{B6}$$

$$\sum_n \mathrm{e}^{\mathrm{i}(\sigma t_n + kUt_n)}\left(A\mathrm{e}^{-\mathrm{i}(\sigma t_n - kUt_n)} + B\mathrm{e}^{+\mathrm{i}\sigma t_n + kUt_n} - F_n\right) \quad = 0 \tag{B7}$$

$$\sum_n t_n \mathrm{Im}\left[\left(A\mathrm{e}^{-\mathrm{i}(\sigma t_n - kUt_n)} + B\mathrm{e}^{\mathrm{i}(\sigma t_n + kUt_n)}\right)\left(A\mathrm{e}^{-\mathrm{i}(\sigma t_n - kUt_n)} + B\mathrm{e}^{+\mathrm{i}(\sigma \boldsymbol{t_n} + kUt_n)} - F_n\right)\right] \quad = 0, \tag{B8}$$

where Im(X) is the imaginary part of X.

Using $t_1=0$, this can be re-arranged as

$$\alpha A + \beta B \quad = \quad \gamma \tag{B9}$$

$$\beta A + \delta B \quad = \quad \gamma' \tag{B10}$$

$$\begin{aligned}\mathrm{Im}\Big[t_2\left(\alpha_2 A + \beta_2 B\right)\cdot\left(\alpha_2 A + \beta_2 B - F_2\right) \\ +t_3\left(\alpha_3 A + \beta_3 B\right)\cdot\left(\alpha_3 A + \beta_3 B - F_3\right)\Big] = 0\end{aligned} \tag{B11}$$

where we have defined

$$\alpha \quad = \quad \left[1 + \mathrm{e}^{-\mathrm{i}(2\sigma - 2kU)t_2} + \mathrm{e}^{-\mathrm{i}(2\sigma - 2kU)t_3}\right] \tag{B12}$$

$$\beta = \left[1 + e^{i2kUt_2} + e^{i2kUt_3}\right] \tag{B13}$$

$$\gamma = F_1 + F_2 e^{-i(\sigma - kU)t_2} + F_3 e^{-i(\sigma - kU)t_3} \tag{B14}$$

$$\delta = \left[1 + e^{2i(\sigma + kU)t_2} + e^{2i(\sigma + kU)t_3}\right] \tag{B15}$$

$$\gamma' = F_1 + F_2 e^{i(\sigma + kU)t_2} + F_3 e^{i(\sigma + kU)t_3} \tag{B16}$$

$$\alpha_2 = e^{-i(\sigma - kU)t_2} \tag{B17}$$

$$\beta_2 = e^{i(\sigma + kU)t_3} \tag{B18}$$

$$\alpha_3 = e^{-i(\sigma - kU)t_3} \tag{B19}$$

$$\beta_3 = e^{i(\sigma + kU)t_3} \tag{B20}$$

We may eliminate A and B from the first two equations giving

$$A = \left(\gamma - \beta B\right) / \alpha, \tag{B21}$$

and

$$B = (\gamma' - \gamma\beta / \alpha) / (\delta - \beta^2 / \alpha). \tag{B22}$$

replacing these expressions for A and B in Equation B11 gives one equation for U,

$$\begin{aligned} f(U, k, \sigma, F_1, F_2, F_3, t_2, t_3) = \mathrm{Im}\Big[& t_2\left(\alpha_2 A + \beta_2 B\right) \times \left(\alpha_2 A + \beta_2 B - F_2\right) \\ & + t_3\left(\alpha_3 A + \beta_3 B\right)\Big) \times \left(\alpha_3 A + \beta_3 B - F_3\right)\Big] = 0. \end{aligned} \tag{B23}$$

Finding the solution for $f = 0$ gives an estimate of the value of U. This operation can be repeated for each Fourier transform (each tile) and each spectral component. Different averaging procedures are discussed in Section 3. In particular, we find that the square root of the sum of $|\varepsilon_n|^2$ is linearly correlated to the error on U, in particular when the phase differences are large. Finally, this approach is easily extended to more than three images.

Acknowledgments
Fabrice Ardhuin and Matias Alday were supported by CNES as part of the SKIM preparation program and ANR grants for ISblue (ANR-17-EURE-0015) and MIMOSA (ANR-14-CE01-0012), with additional support from the European Space Agency, through the IASCO contract 4000129945/19/NL/FF/gp and SARONG contract 4000117644/16/NL/FF/gp. Maria Yurovskaya was supported by the Ministry of Science and Education of the Russian Federation under State Assignment no. 0555-2021-0004 and Russian Science Foundation through Project no. 21-47-00038. The authors thank Bertrand Chapron for fruitful discussions and two anonymous reviewers that have helped make the manuscript much more readable.

Data Availability Statement

The authors acknowledge the use of Copernicus Sentinel-2 data, obtained from the Copernicus Science Hub (https://scihub.copernicus.eu), and buoy data were furnished by the Coastal Data Information Program (CDIP), Integrative Oceanography Division, operated by the Scripps Institution of Oceanography, under the sponsorship of the U.S. Army Corps of Engineers and the California Department of Parks and Recreation (https://doi.org/10.18437/C7WC72).

References

Andrews, D. G., & McIntyre, M. E. (1978). On wave action and its relatives. *Journal of Fluid Mecanics*, *89*, 647–664. https://doi.org/10.1017/s0022112078002785

Ardhuin, F., Chapron, B., Collard, F., Smith, M., Stopa, J., Thomson, J., et al. (2017). Measuring ocean waves in sea ice using SAR imagery: A quasi-deterministic approach evaluated with Sentinel-1 and in situ data. *Remote Sensing of Environment*, *189*, 211–222. https://doi.org/10.1016/j.rse.2016.11.024

Ardhuin, F., Chapron, B., Maes, C., Romeiser, R., Gommenginger, C., Cravatte, S., et al. (2019). Satellite doppler observations for the motions of the oceans. *Bulletin of the American Meterological Society*, *100*. https://doi.org/10.1175/BAMS-D-19-0039.1

Ardhuin, F., Gualtieri, L., & Stutzmann, E. (2015). How ocean waves rock the earth: Two mechanisms explain seismic noise with periods 3 to 300 s. *Geophysical Research Letters*, *42*, 765–772. https://doi.org/10.1002/2014GL062782

Ardhuin, F., Marié, L., Rascle, N., Forget, P., & Roland, A. (2009). Observation and estimation of Lagrangian, Stokes and Eulerian currents induced by wind and waves at the sea surface. *Journal of Physical Oceanography*, *39*(11), 2820–2838. https://doi.org/10.1175/2009jpo4169.1

Ardhuin, F., & Roland, A. (2012). Coastal wave reflection, directional spreading, and seismo-acoustic noise sources. *Journal of Geophysical Research*, *117*, C00J20. https://doi.org/10.1029/2011JC007832

Barrick, D. E. (1977). Extraction of wave parameters from measured HF radar sea-echo Doppler spectra. *Radio Science*, *12*, 415–423. https://doi.org/10.1029/rs012i003p00415

Brekhovskikh, L. M., Goncharov, V. V., Kurtepov, V. M., & Naugolnykh, K. A. (1973). The radiation of infrasound into the atmosphere by surface waves in the ocean. *Izvestiya - Atmospheric and Oceanic Physics*, *9*, 899–907.

Broche, P., de Maistre, J. C., & Forget, P. (1983). Mesure par radar décamétrique cohérent des courants superficiels engendrés par le vent. *Oceanologica Acta*, *6*(1), 43–53.

Campana, J., Terrill, E. J., & Paolo, T. D. (2016). The development of an inversion technique to extract vertical current profiles from X-band radar observations. *Journal of Atmospheric and Oceanic Technology*, *33*, 2015–2028. https://doi.org/10.1175/JTECH-D-15-0145.1

Cronin, M. F., Gentemann, C. L., Edson, J., Ueki, I., Bourassa, M., Brown, S., et al. (2019). Air-sea fluxes with a focus on heat and momentum. *Frontiers in Marine Science*, *6*, 430. https://doi.org/10.3389/fmars.2019.00430

De Carlo, M., Ardhuin, F., & Pichon, A. L. (2020). Atmospheric infrasound radiation from ocean waves in finite depth: A unified generation theory and application to radiation patterns. *Geophysical Journal International*, *221*, 569–585. https://doi.org/10.1093/gji/ggaa015

Drusch, M., Del Bello, U., Carlier, S., Colin, O., Fernandez, V., Gascon, F., & Bargellini, P. (2012). Sentinel-2: Esa's optical high-resolution mission for GMES operational services. *Remote Sensing of Environment*, *120*, 25–36. https://doi.org/10.1016/j.rse.2011.11.026

Elfouhaily, T., Chapron, B., Katsaros, K., & Vandemark, D. (1997). A unified directional spectrum for long and short wind-driven waves. *Journal of Geophysical Research*, *102*(C7), 15781–15796. https://doi.org/10.1029/97jc00467

Elipot, S., Lumpkin, R., Perez, R. C., Lilly, J. M., Early, J. J., & Sykulski, A. M. (2016). A global surface drifter data set at hourly resolution. *Journal of Geophysical Research*, *121*, 2937–2966. https://doi.org/10.1002/2016JC011716

Farrell, W. E., & Munk, W. (2008). What do deep sea pressure fluctuations tell about short surface waves? *Geophysical Research Letters*, *35*(7), L19605. https://doi.org/10.1029/2008GL035008

Fedele, F., Benetazzo, A., Gallego, G., Shih, P.-C., Yezzi, A., Barbariol, F., & Ardhuin, F. (2013). Space-time measurements of oceanic sea states. *Ocean Modelling*, *70*, 103–115. https://doi.org/10.1016/j.ocemod.2013.01.001

Guimarães, P. V., Ardhuin, F., Bergamasco, F., Leckler, F., Filipot, J.-F., Shim, J.-S., et al. (2020). A data set of sea surface stereo images to resolve space-time wave fields. *Scientific Data*, *7*, 145. https://doi.org/10.1038/s41597-020-0492-9

Hasselmann, K. (1963). A statistical analysis of the generation of microseisms. *Reviews of Geophysics*, *1*(2), 177–210. https://doi.org/10.1029/rg001i002p00177

Hogg, D. W., Bovy, J., & Lang, D. (2010). Data analysis recipes: Fitting a model to data. ArXiv. 1008.4686.

Kääb, A., Winsvold, S. H., Altena, B., Nuth, C., Nagler, T., & Wuite, J. (2016). Glacier remote sensing using Sentinel-2. Part I: Radiometric and geometric performance, and application to ice velocity. *Radio Science*, *8*, 598. https://doi.org/10.3390/rs8070598

Kirincich, A. (2016). Remote sensing of the surface wind field over the coastal ocean via direct calibration of HF radar backscatter power. *Journal of Atmospheric and Ocean Technology*, *33*(7), 1377–1392. https://doi.org/10.1175/jtech-d-15-0242.1

Kudryavtsev, V., Yurovskaya, M., Chapron, B., Collard, F., & Donlon, C. (2017a). Sun glitter imagery of surface waves. Part 1: Directional spectrum retrieval and validation. *Journal of Geophysical Research*, *122*, 1369–1383. https://doi.org/10.1002/2016JC012425

Kudryavtsev, V., Yurovskaya, M., Chapron, B., Collard, F., & Donlon, C. (2017b). Sun glitter imagery of surface waves. Part 2: Waves transformation on ocean currents. *Journal of Geophysical Research*, *122*, 1384–1399. https://doi.org/10.1002/2016JC012426

Laxague, N. J. M., Özgökmen, T. M., Haus, B. K., Novelli, G., Shcherbina, A., Sutherland, P., et al. (2018). Observations of near-surface current shear help describe oceanic oil and plastic transport. *Geophysical Research Letters*, *44*, 245–249. https://doi.org/10.1002/2017GL075891

Lebedev, K., Yoshinari, H., Maximenko, N. A., & Hacker, P. W. (2007). *Yomaha'07: Velocity data assessed from trajectories of argo floats at parking level and at the sea surface* (Technical Report No. 4). International Pacific Research Center, University of Hawaii. Retrieved from http://apdrc.soest.hawaii.edu/projects/yomaha/yomaha07/YoMaHa070612small.pdf

Leckler, F., Ardhuin, F., Peureux, C., Benetazzo, A., Bergamasco, F., & Dulov, V. (2015). Analysis and interpretation of frequency-wavenumber spectra of young wind waves. *Journal of Physical Oceanography*, *45*, 2484–2496. https://doi.org/10.1175/JPO-D-14-0237.1

Longuet-Higgins, M. S. (1960). Reflection and refraction at a random moving surface. II. Number of specular points in a Gaussian surface. *Journal of the Optical Society of America*, *50*(9), 845–850. https://doi.org/10.1364/JOSA.50.000845

Lumpkin, R., Özgökmen, T., & Centurioni, L. (2017). Advances in the application of surface drifters. *Annual Review of Marine Science*, *9*, 6.1–6.23. https://doi.org/10.1146/annurev-marine-010816-060641

Lygre, A., & Krogstad, H. E. (1986). Maximum entropy estimation of the directional distribution in ocean wave spectra. *Journal of Physical Oceanography*, *16*, 2052–2060. https://doi.org/10.1175/1520-0485(1986)016<2052:meeotd>2.0.co;2

Mansard, E. P. D., & Funke, E. R. (1980). The measurement of incident and reflected spectra using a least squares method. In Paper presented at the International Conference on Coastal Engineering (Vol. 1). https://doi.org/10.9753/icce.v17.8

Marié, L., Collard, F., Nouguier, F., Pineau-Guillou, L., Hauser, D., Boy, F., et al. (2020). Measuring ocean surface velocities with the KuROS and KaRADOC airborne near-nadir doppler radar: A multi-scale analysis in preparation of the skim mission. *Ocean Science*, *16*, 1399–1429. https://doi.org/10.5194/os-16-1399-2020

Maximenko, N., Corradi, P., Law, K. L., Sebille, E. V., Garaba, S. P., Lampitt, R. S., et al. (2019). Toward the integrated marine debris observing system. *Frontiers in Marine Science*, *6*, 447. https://doi.org/10.3389/fmars.2019.00447

Niiler, P. P., & Paduan, J. D. (1995). Wind-driven motions in the Northeast Pacific as measured by Lagrangian drifters. *Journal of Physical Oceanography*, *25*(11), 2819–2930. https://doi.org/10.1175/1520-0485(1995)025<2819:wdmitn>2.0.co;2

Nouguier, F., Guérin, C.-A., & Chapron, B. (2009). "Choppy wave" model for nonlinear gravity waves. *Journal of Geophysical Research*, *114*(C09), C09012. https://doi.org/10.1029/2008JC004984

Novelli, G., Guigand, C. M., Cousin, C., Ryan, E. H., Laxague, N. J. M., Dai, H., et al. (2017). A biodegradable surface drifter for ocean sampling on a massive scale. *Journal of Atmospheric and Oceanic Technology*, *34*, 2509–2532. https://doi.org/10.1175/JTECH-D-17-0055.1

Peureux, C., Benetazzo, A., & Ardhuin, F. (2018). Note on the directional properties of meter-scale gravity waves. *Ocean Science*, *14*, 41–52. https://doi.org/10.5194/os-14-41-2018

Quilfen, Y., & Chapron, B. (2019). Ocean surface wave-current signatures from satellite altimeter measurements. *Geophysical Research Letters*, *216*, 253–261. https://doi.org/10.1029/2018GL081029

Rio, M.-H., Mulet, S., & Picot, N. (2014). Beyond GOCE for the ocean circulation estimate: Synergetic use of altimetry, gravimetry, and in situ data provides new insight into geostrophic and Ekman currents. *Geophysical Research Letters*, *41*, 8918–8925. https://doi.org/10.1002/2014GL061773

Rodríguez, E., Wineteer, A., Perkovic-Martin, D., Gál, T., Stiles, B. W., Niamsuwan, N., & Monje, R. R. (2018). Estimating ocean vector winds and currents using a Ka-band pencil-beam doppler scatterometer. *Remote Sensing*, *4*, 576. https://doi.org/10.3390/rs10040576

Stewart, R. H., & Joy, J. W. (1974). HF radio measurements of surface currents. *Deep Sea Research and Oceanographic Abstracts*, *21*, 1039–1049. https://doi.org/10.1016/0011-7471(74)90066-7

Sutherland, G., Marié, L., Reverfdin, G. (2016). Enhanced turbulence associated with the diurnal jet in the ocean surface boundary layer. *Journal of Physical Oceanography*, *46*(10), 3051–3067. https://doi.org/10.1175/JPO-D-15-0172.1

Suzuki, N. (2019). On the physical mechanisms of the two-way coupling between a surface wave field and a circulation consisting of a roll and streak. *Journal of Fluid Mechics*, *881*, 906–950. https://doi.org/10.1017/jfm.2019.752

Teague, C. C., Vesecky, J. F., & Hallock, Z. R. (2001). A comparison of multifrequency HF radar and ADCP measurements of near-surface currents during COPE-3. *IEEE Journal of Oceanic Engineering*, *26*(3), 399–405. https://doi.org/10.1109/48.946513

Tyler, G. L., Teague, C. C., Stewart, R. H., Peterson, A. M., Munk, W. H., & Joy, J. W. (1974). Wave directional spectra from synthetic aperture observations of radio scatter. *Deep Sea Research and Oceanographic Abstracts*, *21*, 989–1016. https://doi.org/10.1016/0011-7471(74)90063-1

Villas Bôas, A. B., Cornuelle, B. D., Mazloff, M. R., Gille, S. T., & Ardhuin, F. (2020). Wave-current interactions at meso and submesoscales: Insights fromidealized numerical simulations. *Journal of Physical Oceanography*, *50*(12), 1–45. https://doi.org/10.1002/2016JC012413

Weber, B. L., & Barrick, D. E. (1977). On the nonlinear theory for gravity waves on the ocean's surface. Part I: Derivations. *Journal of Physical Oceanography*, *7*, 3–10. https://doi.org/10.1175/1520-0485(1977)007<0003:otntfg>2.0.co;2

Wunsch, C., & Ferrari, R. (2009). Ocean circulation kinetic energy: Reservoirs, sources, and sinks. *Annual Reviews of Fluid Mechanics*, *41*, 253–282. https://doi.org/10.1146/annurev.fluid.40.111406.102139

Young, I. R., Rosenthal, W., & Ziemer, F. (1985). A three-dimensional analysis of marine radar images for the determination of ocean wave directionality and surface currents. *Journal of Geophysical Research*, *90*, 1049–1059. https://doi.org/10.1029/jc090ic01p01049

Yurovskaya, M., Kudryavtsev, V., Chapron, B., & Collard, F. (2019). Ocean surface current retrieval from space: The sentinel-2 multispectral capabilities. *Remote sensing of Environment*, *234*, 111468. https://doi.org/10.1016/j.rse.2019.111468

Zelt, J. A., & Skjelbreia, J. E. (1993). Estimating incident and reflected wave fields using an arbitrary number of wave gauges. In Paper presented at the 1992 International Conference on Coastal Engineering (Vol. 1). https://doi.org/10.1061/9780872629332.058